Pergamon

*Journal of Structural Geology*, Vol. 18, No. 5, pp. 657 to 671, 1996

0191-8141/96 $15.00 + 0.00

0191-8141(95)00119-0

# Formation of voids and veins during faulting

STEPHEN R. BROWN

Geomechanics Department, Sandia National Laboratories, Albuquerque, NM 87185-0751, U.S.A.

and

RONALD L. BRUHN

Department of Geology and Geophysics, University of Utah, Salt Lake City, UT 84112-1183, U.S.A.

(*Received* 8 *August* 1994; *accepted in revised form* 15 *September* 1995)

**Abstract**—We have developed a quantitative model of void and vein development in fault zones based on observations of fault roughness and the contact characteristics of rough, directionally anisotropic fractal surfaces. This model includes progressive dilation of the fault during slip events and the elastic deformation of the surfaces normal to the fault plane (closure) as new void space develops. The model predicts vein geometries that are qualitatively similar to those observed in fault-controlled mineral deposits. The statistics of the vein system are described and strategies for sampling of such structures by drilling are developed. The results have significant implications for evaluation of ore reserves and evaluating the fluid transport properties of faults. Copyright © 1996 Elsevier Science Ltd

## INTRODUCTION

Structures in fault zones affect the generation and propagation of earthquake ruptures (Sibson 1989), the flow of groundwater and hydrocarbons (Smith *et al.* 1990, Knipe 1993), and play an important role in the origin of mineral deposits (Newhouse 1940). Roughness of fault surfaces influences rupturing by affecting fluid transport properties, frictional coefficients and rupture propagation energy. Mismatch between ridges and furrows on opposite sides of fault surfaces creates channeling of fluid flow and formation of void space for fluid entrapment and vein deposition. Alternatively, penetration of opposing surfaces generates attrition breccia, and these sites form strong patches or asperities within the fault zone because fresh rock must be broken to accommodate further displacement.

Frictional properties of faults are affected by roughness at scales less than 1 m (Scholz 1988, Power & Tullis 1992), but rupture propagation, large-scale fluid channeling and the formation of mineral deposits may be affected by roughness at length scales of decameters or more. Many years ago, Gilbert (1928) suggested that bedrock ridges or spurs, with spatial scales up to kilometers, form in the hanging walls of normal faults above bumps in the primary fault surface. Mineralized vein systems develop in dilational cavities that vary in dimension from millimeters to decameters, but the latter scale is probably most important as the site of commercially exploitable ore (Newhouse 1940).

We have developed a quantitative model of void and vein development in fault zones based on observations of fault roughness and the contact characteristics of rough, directionally anisotropic fractal surfaces. This model includes progressive dilation of the fault during slip events and the elastic deformation of the surfaces normal to the fault plane (closure) as new void space develops. The model predicts vein geometries that are qualitatively similar to those observed in fault-controlled mineral deposits. The statistics of the vein system are described and strategies for sampling of such structures by drilling are developed. The results have significant implications for evaluation of ore reserves and evaluating the fluid transport properties of faults.

In what follows we present field observations on the character of faults and associated vein systems. We then use this information to develop a mathematical model of rough-walled fault surfaces and show the properties of such a fault under varying shear offset and normal stress.

## FIELD OBSERVATIONS

### *Fracture and joint surfaces*

Measurements and analysis of surface profiles of natural fractures have established that fracture surface topography can be represented in terms of fractal geometry (Brown & Scholz 1985, Power *et al.* 1987, Power & Tullis 1991, 1992, Brown 1995). Topographic profiles are treated as spatial series, and Fourier analysis (especially the power spectrum) is used to analyze their properties. The power spectrum is computed by breaking a time or spatial series, in this case the profile, into a sum of sinusoidal components: each with its own wavelength, amplitude and phase (Fig. 1). The squared amplitude of

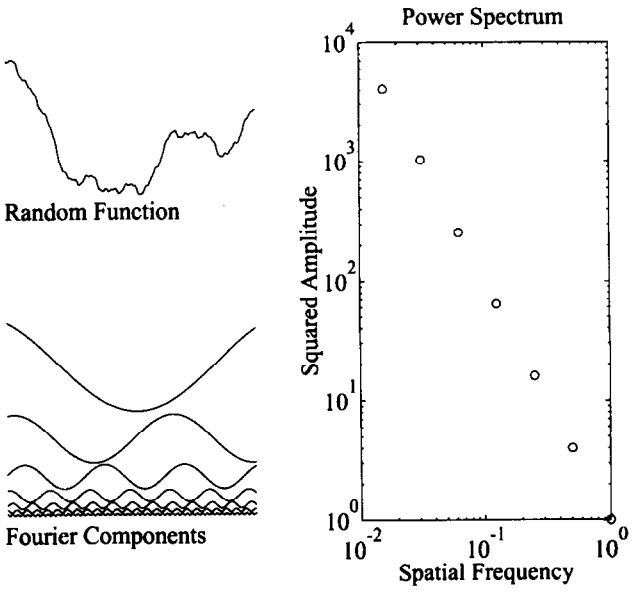


Fig. 1. Illustration of the power spectrum of a surface profile. The surface profile (irregular curve, upper left) is decomposed into a series of sinusoidal components (lower left). Each component is characterized by its wavelength ($\lambda$), amplitude ($A$) and phase (relative position of the first peak of the sinusoid to that of all others). A plot of the power $A^2$ vs the spatial frequency $1/\lambda$ for all sinusoidal components is known as the power spectrum (graph on the right).

each component is referred to as its power and a plot of power vs wavenumber or inverse of wavelength is referred to as the power spectrum. The phase indicates the position of the first peak of each sinusoid relative to all others. The phase spectrum is a plot of the phase as a function of wavenumber. Phase spectra for rough surfaces are typically random, that is there is no consistent relation between phase and wavenumber. The power per unit frequency interval is known as the power spectral density. Excellent introductions to spectral analysis are given by Bendat & Piersol (1971) and Båth (1974).

Linear profiles of fracture and joint surface profiles exhibit power spectral density functions of the form:

$$G(k) = Ck^{-\alpha}, \quad (1)$$

indicating self-affine fractal geometry (Mandelbrot 1983). Here, $k$ is the wavenumber related to the wavelength $\lambda$ according to $k = 2\pi/\lambda$. The exponent $\alpha$ depends on the fractal dimension of a surface $D$ as $\alpha = 7 - 2D$. The fractal dimension of a linear profile is simply $D_p = D - 1$. The fractal dimension describes the proportion of high frequency to low frequency roughness and is a measure of surface texture. For natural fracture surfaces, $D$ falls in the range $2 \leq D \leq 3$, with small values representing smoother surfaces. The constant $C$ determines the standard deviation of the surface roughness about its mean plane at a particular reference profile length. Additionally, the two surfaces comprising a fracture are often closely matched at long wavelengths and mismatched at small wavelengths, resulting in an aperture distribution whose spectrum has the form of equation (1) at small wavelengths, but flattens out at long wavelengths (Brown & Scholz 1986, Power & Tullis 1992, Brown 1995).

*Fault surfaces*

Studies of fault surfaces over a variety of scales lead to a fractal description of the roughness similar to that for fractures and joints (Scholz & Aviles 1986, Power *et al.* 1987, Bruhn *et al.* 1991, Power & Tullis 1991, Lee & Bruhn 1992). Below we provide some additional details of and evidence for this description.

Lee & Bruhn (1992) made a detailed outcrop study of fault anisotropy on normal fault surfaces from several rock types. They found that surface properties of natural faults are complex, with amplitude to wavelength scaling and fractal dimension a function of direction along the fault surface, and also dependent on overall scale. They suggest that fault topography is roughly self-affine at wavelengths between 1 mm and 5 km, with a general decrease in fractal dimension as a function of increasing wavelength. They note anisotropy in the roughness measured by an azimuthal variation in the ratio of amplitude to wavelength of the fault topography. This ratio varies from 2.0 to 4.5 for the faults measured in their study. The long-axis of topographic grain is aligned parallel to slip direction. They find that $D$ varies from approximately 1.5 at the 10 cm scale to 1.25 at the several meter scale. At longer wavelengths $D$ varies between 1.1 and 1.0.

The sinuous traces of faults and scarps on geological maps reflect the complex interaction between erosional topography and corrugated fault surfaces (Scholz & Aviles 1986, Bruhn *et al.* 1991). Although fault traces may be corrected for the effects of erosional topography, the resulting profiles yield little information on the extent and nature of the corrugated structure in the subsurface. Exposures of faults in outcrop show spectacular, corrugated topography in many cases, but the exposures are limited to dimensions of several tens of meters at most. Geological maps constructed during mining of fault controlled ore deposits provide structural information at scales up to several hundred meters, a much larger area than observed in outcrop, and provide subsurface information that is not available from ordinary geological maps (Fig. 2).

Openings generated by sliding of currugated fault surfaces are recognized as a critical element in the formation of veins in fault-controlled ore deposits (Newhouse 1940). We selected maps and vein measurements from several deposits to generate appropriate parameters for fractal modeling (Table 1).

Examples from reverse faults include mesothermal quartz-gold veins of the Mother Lode District, California (Knopf 1929) and Talkeetna Mountains, Alaska (Stoll 1940, Ray 1954). The localization of epithermal *Pb*, *Zn*, *Au* and *Ag* in void space and breccia generated during fault slip is well documented in normal faults from the Slocan District, British Columbia (Roscoe 1951), the Mogollon District, New Mexico (Ferguson 1927), and the Daisy Mine, Utah (Wu & Bruhn 1994).

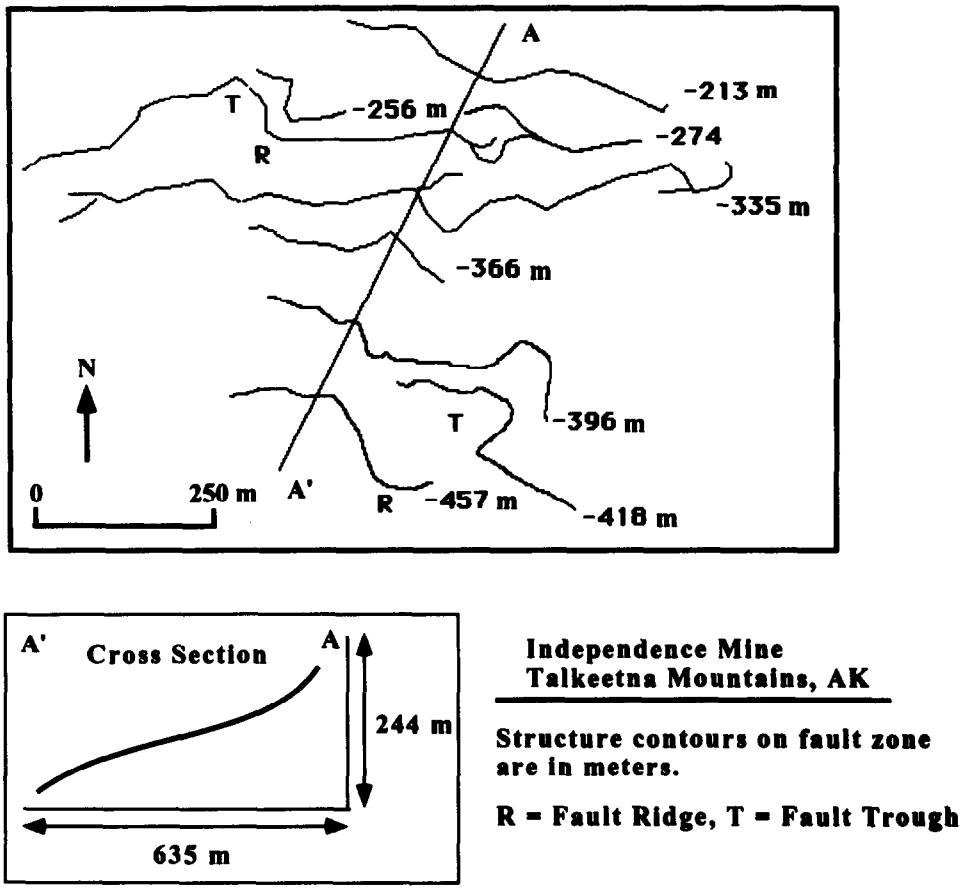


Fig. 2. Mine map of the Independence reverse fault quartz–gold vein deposit, Talkeetna Mountains, Alaska. Each trace represents a structure contour on the fault and vein system. The cross-section illustrates the general shape of the fault and vein system along line A–A'. Mine data after Ray (1954).

Similar deposits occur in strike slip faults of the La Plata District, CO (Eckel 1949).

Mine maps of fault controlled ore deposits show the trace of the fault at different levels below the Earth's surface (Fig. 2). These maps record the sinuousity of the faults, and can be used to compute the standard deviation and amplitude of the fault sinuosity at scales between a few meters and hundreds of meters. The maps are not adequate, however, for determination of the fractal dimension because they provide accurate information on spatial scaling only over 1–2 orders of magnitude at best. For this reason, we use the results of studies with more detailed measurements of fault surface roughness to assign a 'typical' fractal dimension for modeling purposes (Power *et al.* 1987, Lee & Bruhn 1992).

The fault profile data in Table 1 is used to ensure that the amplitude scaling (amplitude to fault profile length ratio) of the model fault roughness is consistent with that observed in natural fault zones. The true amplitudes or sinuousity of the mapped faults is found as follows: we digitize the fault traces, find the average strike and dip of the fault by fitting a plane through the traces using linear, least-squares regression, and generate a profile of the fault on each mine level. Each profile is the deviation of the fault surface about the mean plane at the depth of a specific mining level. Critical parameters for creating fractal models of fault surfaces include the peak to peak amplitude, standard deviation of amplitudes, and the profile length (Table 1). The profiles are essentially perpendicular to direction of slip for reverse and normal faults, but parallel to slip direction for strike slip faults. The ratio of peak-to-peak amplitude to profile length is 0.1–0.01 for profiles that are up to several hundred meters long. These values are about the same as (or only a bit larger than) those found on several slip-perpendicular fault profiles (less than 10 m long) by Power and Tullis (1991).

The anisotropy of fault surfaces is defined by elongate topography which mostly parallels the direction of slip. Anisotropy is documented by profiling a fault surface in at least two directions, one parallel and the other perpendicular to slip (Power *et al.* 1987, Power & Tullis 1991, 1992), and comparing the ratio of profile amplitude at specific wavelengths between profiles. Lee & Bruhn (1992) made a detailed study of fault anisotropy on normal fault surfaces from several rock types, and found that the ratio of amplitude to wavelength varies systematically as a function of direction. Although variable, the ratio of amplitude to wavelength is on average, about 2.5:1 between the slip perpendicular and slip parallel directions. These measurements are limited to outcrops, and therefore restricted to scales of tens of meters and smaller. However, contour maps of fault structures in mines (Roscoe 1951) suggest that an anisotropy of 2.5:1 is also representative at scales greater than 100 m, which is the spatial range of our fractal models.

Table 1. Fault parameters determined from mine maps

| Mine level | Amplitude (+) | Amplitude (−) | SD | Profile length | Total amplitude length |
|---|---|---|---|---|---|
| Independence mine, Talkeetna Mountains, Alaska (reverse fault) (Strike parallel profiles from map by Ray 1954) | | | | | |
| −213 | 7.18 | −10.33 | 4.95 | 227.30 | 0.08 |
| −256 | 5.87 | −7.88 | 4.35 | 87.09 | 0.16 |
| −274 | 17.74 | −18.76 | 7.75 | 522.70 | 0.07 |
| −292 | 8.90 | −6.06 | 4.29 | 138.80 | 0.11 |
| −335 | 9.92 | −14.27 | 5.03 | 553.20 | 0.04 |
| −365 | 7.30 | −7.75 | 3.33 | 175.50 | 0.09 |
| −381 | 3.71 | −5.15 | 1.70 | 146.00 | 0.06 |
| −396 | 19.41 | −16.07 | 9.66 | 351.40 | 0.10 |
| −457 | 19.00 | −19.86 | 9.50 | 269.00 | 0.14 |
| | Average values | | 5.62 | 274.55 | 0.09 |
| Daisy Mine, Oquirrh Mountains, Utah (normal fault) (Strike parallel profiles from map provided by T. Shrier, unpublished data) | | | | | |
| Mine level | Amplitude (+) | Amplitude (−) | SD | Profile length | Total amplitude/length |
| −91 | 2.97 | −2.63 | 1.50 | 134.00 | 0.04 |
| −122 | 6.00 | −4.52 | 2.03 | 200.00 | 0.05 |
| −152 | 5.58 | −3.28 | 1.89 | 116.00 | 0.08 |
| −160 | 5.64 | −3.91 | 2.28 | 174.00 | 0.05 |
| −213 | 7.05 | −3.67 | 2.08 | 434.00 | 0.02 |
| | Average values | | 1.96 | 211.60 | 0.05 |
| Rambler Fault, Slocan Mining District, British Columbia (normal fault) (four profiles generated parallel to fault slip direction from contour map by Roscoe 1951) | | | | | |
| Profile | Amplitude (+) | Amplitude (−) | SD | Profile length | Total amplitude/length |
| A (slip paral.) | 15.30 | −5.31 | 4.06 | 340.00 | 0.06 |
| B (slip paral.) | 14.88 | −6.38 | 5.30 | 344.00 | 0.06 |
| C (slip perp.) | 12.93 | −17.45 | 8.86 | 227.00 | 0.14 |
| D (slip perp.) | 8.07 | −5.53 | 3.35 | 227.00 | 0.06 |
| Plymouth Mine, Mother Lode District, California (reverse fault) (dip-parallel profile of hanging wall contact illustrated in Knopf 1929) | | | | | |
| Profile | Amplitude (+) | Amplitude (−) | SD | Profile length | Total amplitude/length |
| Down-dip | 0.70 | −0.81 | 0.38 | 48.00 | 0.03 |
| La Plata Mine, Colorado (transcurrent fault) (from map by Eckel 1949) | | | | | |
| Mine level | Amplitude (+) | Amplitude (−) | SD | Profile length | Total amplitude/length |
| −30 | 3.64 | −3.31 | 2.00 | 116.00 | 0.06 |

Note: All units are in meters, and all profile amplitudes are deviations from a best-fit plane to the fault zone.

The fractal dimension of most natural surfaces lies in the range $2.0 \leq D \leq 2.3$ (Brown & Scholz 1985, Power *et al.* 1987, Power & Tullis 1991, 1992). Recent field studies by Lee & Bruhn (1992) find that the fractal dimension of normal fault surfaces is a function of profile length. The dimension is in the range $2.2 \leq D \leq 2.3$ for centimeter to meter length profiles. The longest profiles made by directly measuring individual fault surfaces are several tens of meters long, and at this scale the fractal dimension falls in the range $2.1 \leq D \leq 2.2$. At a scale of hundreds of meters to kilometers as measured on geologic and mine maps the dimension falls in the range $2.0 \leq D \leq 2.1$. At these largest scales the resolution is poor and the 'fault' traces may actually partly reflect the intersection and linking together of several fault surfaces rather than the topography of an individual surface. We use $D = 2.2$ for modeling purposes, a value roughly in the center of the range for profiles centimeters to tens of meters long.

The total displacement on the faults studied (Table 1) is estimated at tens to hundreds of meters. The amount of slip per event is not known in most cases. Often vein deposition is episodic, as inferred by the compound nature of veins containing breccia bodies and slices of wall rock. Robert & Boullier (1993) suggest that for a few well-defined cases, single event displacement on some Val d'Or reverse faults is approximately 0.5–2 cm per event. This amount of slip, together with the spatial scale of the Val d'Or faults, is consistent with generation of small to moderate earthquakes, perhaps on the order of $\mathbf{M} = 3$ or less (F. Robert personal communication). We assume that values between 1 and 10 cm per event would be appropriate for the purpose of modeling the formation of a typical fault-controlled ore deposit, because the size and cumulative displacement of Val d'Or reverse faults are similar to those cited in Table 1. However as shown in a later example, larger displacements per slip event could also be considered to investi-

gate the scaling of void space generation over a range of earthquake magnitudes.

*Vein morphology*

Veins in fault zones and surrounding wall rock are generated by a number of processes, including dynamic and quasi-static fracture propagation and fluid infiltration, and the abrupt influx of hot, ascending fluids as fracture permeability is enhanced by rupturing of corrugated fault surfaces (Newhouse 1940, Sibson 1989). Here, our focus is on veins generated during fault slip by the filling of newly opened voids, rather than on secondary veins that are preferentially oriented with respect to the regional stress field, and presumably develop in the interseismic period.

Several structural properties of natural vein systems must be at least partially simulated by a viable fault model. These include both the structure of the fault–vein system as a whole, which is generated by multiple faulting and mineralizing events, and the structural characteristics of individual veins that form as the result of a single faulting and fluid influx event. The cumulative vein thickness is a combination of material added during episodic void formation as well as structural disruption, overlapping and distention of pre-existing vein material.

The following general observations of fault controlled vein systems have been made (Knopf 1929, Newhouse 1940, Stoll 1940, Eckel 1949, Roscoe 1951, Ray 1954, Peters 1993, Robert & Boullier 1993). Fault-controlled vein systems are undulating, tabular to pipe-like bodies composed of both intact and brecciated vein minerals, and slices of hydrothermally altered wall rock. Vein width varies from nearly zero to more than 10 m in some deposits, exhibiting an overall 'pinch and swell' geometry when viewed in cross-section. Lateral extent, like thickness, is highly variable and ranges from small centimeter scale pods to undulating tabular layers that can be traced for hundreds of meters to kilometers. Faults occur as both single and multiple branches and strands, that cut up and down through the vein system, and locally cut into the footwall, bypassing the vein margins until the fault cuts back into the vein. Fault surfaces occur in various locations along the extent of a given vein; sometimes directly along one margin or the other or sometimes through the vein interior. Cross-cutting relationships observed between faults and cemented breccia and gouge zones indicate that the fault system evolved with time. This braided and duplex fault pattern partly explains the observed spatial variability in vein width. Veins presumably become thickened by structural overlap, or thinned by offlap of vein material, depending on the direction of tectonic transport and the angle at which a fault strand cuts across the vein system. Blocks of wall rock are incorporated into the interior of the vein system where fault strands located in the wall rock cut back into the vein in the direction of tectonic transport. Contour lines of vein thickness on dilation maps are mostly elongated in the direction of fault slip, presumably reflecting the anisotropy of the corrugated fault surfaces. But in some areas thickness contours are oriented at high angle to slip direction. This may reflect vein thickness variations resulting from dilation (gaps opened) from either movement on the braided and branching fault system, or by abrupt bending of fault surfaces at lithologic contacts and where subsidiary faults intersect the main fault zone.

The fault–vein system is composed of numerous individual veins and whisker-like veinlets that form where mineral-rich fluids move along larger fractures and infiltrate brecciated rock (Knopf 1929, Stoll 1940, Boullier & Robert 1992). Inspection of outcrops, published photographs and thin sections suggest that the thickness of individual veins is mostly in the sub-millimeter to centimeter range, with a thickness to length ratio of 0.01–0.001. Remnants of individual veins appear as thin, wispy discolored laminae and lenses to the naked eye. Truncation of laminae against one another provides evidence for episodic faulting and fluid influx (Fig. 3). Ore bearing fluid is usually introduced only during part of the faulting history, so that much of the composite vein system consists of barren minerals (Knopf 1929, Newhouse 1940, Stoll 1940). This has major implications for predicting ore grade based on a geostatistical analysis of vein geometry. Ore grade is often not strongly correlated with vein system thickness, a hypothesis that has been borne out by bitter experience (Knopf 1929, Ray 1954). Recently, however, Sanderson *et al.* (1994) have found empirical relationships between ore grade and the distribution function describing cumulative vein thickness. In that study, high ore grade is associated with zones having large numbers of thick veins relative to thin veins. An interpretation of this observation is that the large-thickness veins must also be longer and therefore more likely to be interconnected hydraulically with remote sources of ore-bearing fluids. The assumption of long veins being thicker is based on empirical observations relating fault slip to fault length by Scholz & Cowie (1990). The model of rough faults proposed below leads to this same result.

## MODEL OF ROUGH-WALLED FAULTS

The observation that fracture and fault surfaces are fractal immediately leads to a method for generating simulated surfaces on the computer. The method we use for generating fractal surfaces is described in detail by Brown (1995). This method is summarized briefly below.

One method of computing the power spectral density function described earlier is to take the Fourier transform of profiles of the surface topography (e.g. Bendat & Piersol 1971). This calculation results in a series of sinusoidal components, which can be characterized by their wavelength, amplitude, and relative phase (Fig. 1). This information, collectively known as the amplitude spectrum, is a series of complex numbers which contains both amplitude and phase information.

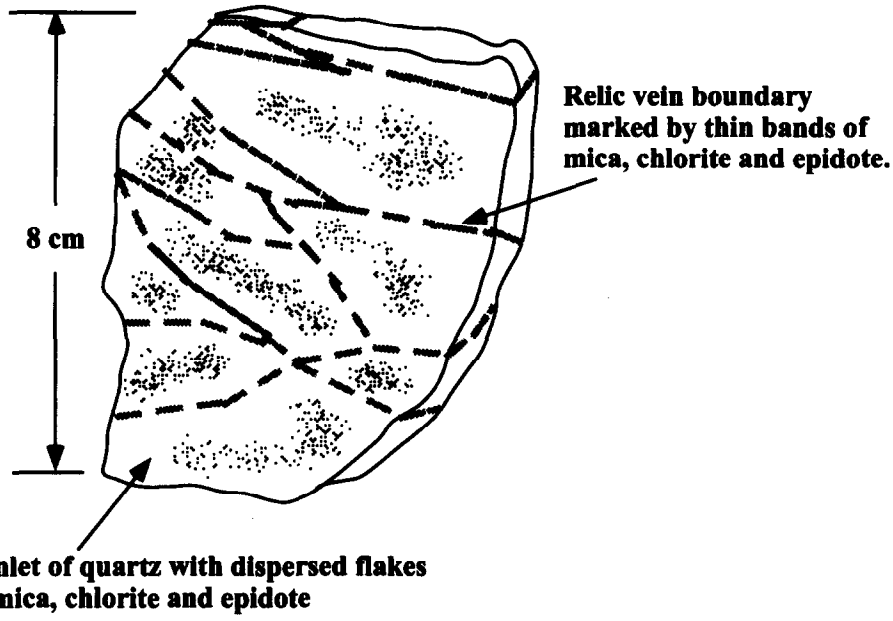


Fig. 3. Sketch of hand sample sized slab of the gold-bearing quartz vein in the Independence Mine, Alaska. The quartz vein is located in a reverse fault. Note the multiple, truncated vein boundaries which indicate several episodes of fluid flow and mineralization.

Brown (1995) presented a spectral synthesis method to generate computer models of both directionally isotropic and anisotropic fractal surfaces. The method works by constructing a two-dimensional complex amplitude spectrum which obeys equation (1) and in addition has a random-phase component (i.e. no deterministic relationship between phase and spatial frequency). The fractal surface is just the inverse Fourier transform of this complex amplitude spectrum. The standard deviation of the surface height is set after the inverse transform is taken.

We wish to consider the effect of directionally anisotropic roughness on void development along a fault. Therefore, we use the spectral synthesis method described briefly above, but with equation (1) modified to include anisotropy as follows:

$$G(k) = C[(k_x/a)^2 + (k_y b)^2]^{-(3.5-D)}. \qquad (2)$$

The ratio $b/a$ is the degree of anisotropy. For $b/a < 1$ the anisotropy is transverse to $x$; for $b/a = 1$ the surface is isotropic, and for $b/a > 1$ the anisotropy is parallel to $x$. In this model the surface has the same fractal dimension in all directions (i.e. the same proportional change in amplitude with a corresponding change in frequency), but at each wavelength the absolute amplitude of the sinusoidal components differ by a constant factor in each direction. Another possible type of anisotropy suggested by the field measurements of Lee & Bruhn (1992) is where the fractal dimension varies with orientation angle, i.e. $D = D(\theta)$ where $\theta = \arctan(k_y/k_x)$. While this possibility is easily implemented in equation (2), it is not considered further here since it is not clear at this time which model of anisotropy is the best.

To force two surfaces of a fracture or fault to be matched at long wavelengths, the two surfaces could be generated with the same random number seed and anisotropy factor, but the random phase spectrum being identical at wavelengths only above a particular value. The length scale at which the phase spectra of the two surfaces become different would be chosen as a fraction of the total surface size. With this modification in the phase spectrum, the power spectrum of the resulting fracture aperture closely resembles that observed for natural fractures and joints (Brown 1995). Examples of surfaces generated by this method are shown in Fig. 4.

## GEOMETRIC MODEL OF VOID DEVELOPMENT

In nature, a fault slips through a complex process including shearing off of asperities, secondary faulting, brecciation and injection of cataclastic material into new voids. Fault surfaces are subsequently modified by the deposition and dissolution of vein minerals caused by chemical disequilibrium between fluid and wall rock. Modification of fault surfaces by these physical and chemical processes is mathematically intractable, so we use a much simplified procedure to create and slip each new generation fault surface. In our model we consider only the geometric and elastic components of void formation and deformation. A discussion of the limits of applicability of these assumptions appears at the end of this section.

To understand the model, the following point of clarification may be necessary. Many discussions of vein fillings (e.g. p. 241 of Ramsay & Huber 1983) consider the case of vein growth contemporaneous with slow (quasi-static) void opening. Here we consider *rapid* opening due to fault slip and *subsequent* filling.

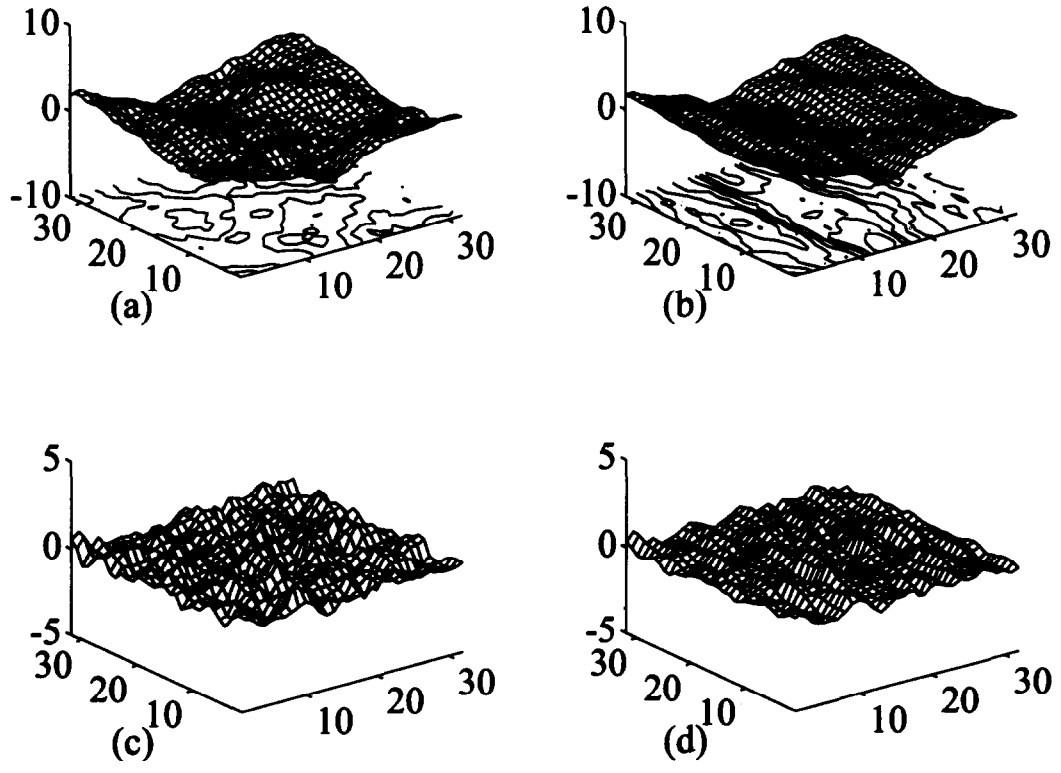


Fig. 4. Examples of surfaces and apertures generated with the fractal algorithm of Brown (1995). The scales on all three axes are in grid units, indicating both distance (units of length) in the fault plane and topographic height normal to the fault plane. (a) Isotropic surface with fractal dimension $D = 2.2$. (b) Anisotropic surface with dimension $D = 2.2$ and anisotropy parameters $b = 3$, $a = 1$. (c) Aperture distribution formed by contact of isotropic surface (a) with another similar surface. Surfaces are mismatched at wavelengths smaller than one-quarter of the total surface size shown. (d) Aperture distribution formed by contact of anisotropic surface (b) with another surface mismatched at one-quarter of the total surface size. Note that the aperture distribution takes on an anisotropic character as well.

*Undeformed aperture: zero effective normal stress*

At the initiation of slip assume that the two opposing fault surfaces are anisotropic fractals and match each other exactly (i.e. are mirror images). Slip occurs parallel to the major axis of the anisotropy. We assume that at first the surfaces, since they are rough, will over-ride one another resulting in the surfaces being propped apart by those asperities with wavelengths on the order of the slip increment. We ignore any damage accrued during the wear processes accompanying slip. The problem, then, is a geometric one of pulling the surfaces apart, offsetting them by the amount of slip, then placing them back together until they touch. Examples of the aperture or void distribution thus formed between the two surfaces are given in Fig. 5. In what follows, we consider the properties of the aperture distribution under zero effective normal stress (i.e. undeformed). Following that, we will discuss the problem of closing the void space by applying a normal load.

*Texture of aperture.* The void distribution formed in this way has the following properties. The aperture, when viewed in three dimensions, contains a dominant texture. Variations in the amplitude (pinching and swelling) of the aperture are almost periodic, that is amplitude variations are repeated in a statistical sense throughout the fracture plane. The aperture distribution is statistically stationary at length scales larger than the amount of slip. The bumps formed by aperture highs, for example, are anisotropic with the long axis of the anisotropy parallel to that of the original surfaces. Both the wavelength and amplitude of these features are determined by the amount of shear offset between the surfaces (Fig. 5).

*Probability density function.* The probability density function for the aperture generated by the contact of two fractal surfaces offset in shear is nearly Gaussian in shape (Fig. 6a). The Gaussian distribution is a symmetric 'bell-shaped' curve which is described completely by the mean and the standard deviation. One of the first questions we can ask is how the mean and standard deviation of this distribution vary with shear offset of the two surfaces. Figure 6(b) shows the results.

*Variogram.* The variogram is widely used in geostatistics to evaluate the degree of spatial correlation between pairs of measurements separated by a specified distance or lag. The variogram of a profile $z(x)$ is defined as:

$$\gamma(\tau) = \lim_{L\to\infty} \int_{-L/2}^{L/2} [z(x+\tau) - z(x)]^2 \, dx, \qquad (3)$$

where $x$ is horizontal distance, $\tau$ is the lag and $L$ is the length of the profile. Examples of the variogram of the aperture as a function of shear offset are shown in Fig. 7.

A feature of significance in many variograms is the

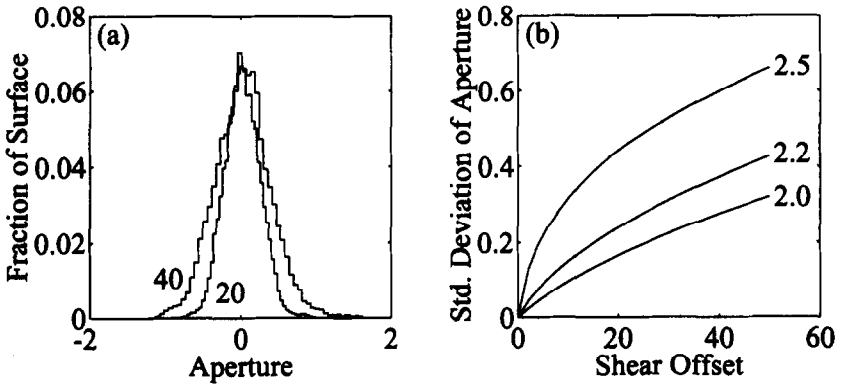


Fig. 6. Examples of the probability distribution for aperture heights created by shear offset of two fractal surfaces with anisotropy of 3:1. Offset is parallel to the greatest principal axis of anisotropy. (a) Probability density functions for shear offsets of 20 and 40 units in a 256 × 256 fault. Fractal dimension is $D = 2.2$. (b) Dependence of standard deviation of roughness on shear offset for fractal dimensions of $D = 2.0$, 2.2 and 2.5. Aperture is expressed in units of the standard deviation of the surface heights at a length scale of 256.

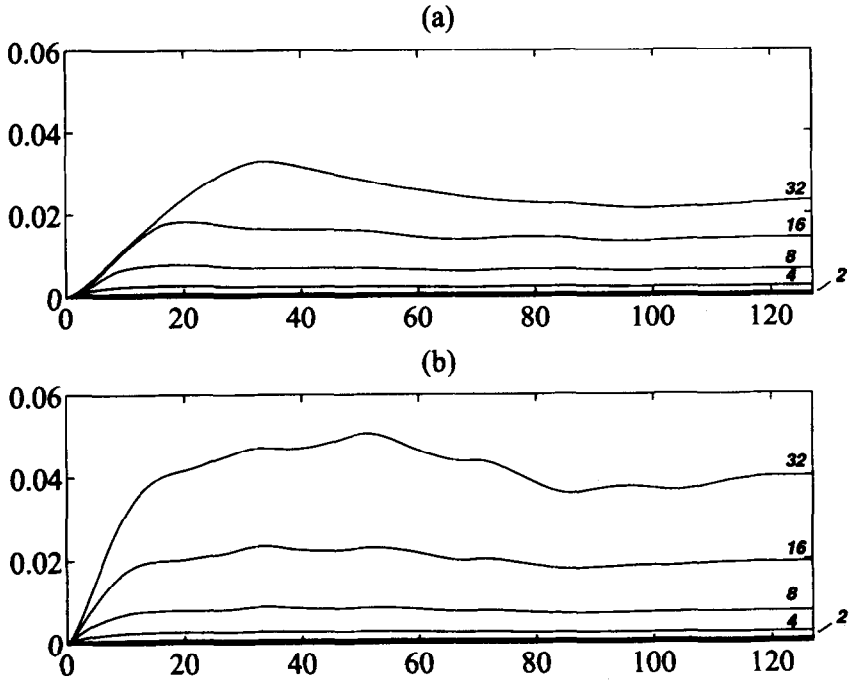


Fig. 7. Example variograms for aperture profiles created by shear offset of two fractal surfaces with a fractal dimension of $D = 2.2$ and anisotropy of 3:1. Offset is parallel to the principal axis of anisotropy. Plot (a) represents profiles parallel to the slip direction and plot (b) represents profiles perpendicular to slip. Horizontal axis is the lag, $\tau$, in grid units. The vertical axis is the variogram normalized by the variance of the individual contacting surfaces at a length scale of 256 grid units $\gamma/\sigma_s^{256}$. Labels 2,4,8,16 and 32 shown to the right identify the amount of shear offset for each curve in numbers of grid units. The profile length used for the calculation is 128 grid units. Note that variance parallel to slip is consistently lower than that perpendicular to slip, the constant value of variance reached at large lag 'sill' increases with shear offset, and the lag at which the sill is reached increases with shear offset.

'sill'. The sill is the area in which the variance becomes about equal to the variance for the data set as a whole. This implies that the data are not correlated at spacings greater than the range where the sill begins. Figure 7 shows that the variograms representing profiles of aperture distributions created by slip between fractal surfaces have well-defined sills. The range at which the sill is reached is a function of the amount of shear offset and the direction relative to the anisotropy of the surface roughness and the slip direction. At length scales larger than where the sill is reached, the aperture becomes a statistically stationary random function.

*Elastic closure of voids under normal stress*

When a normal load is applied to a rough-walled fracture or fault, one may expect closure consisting of both elastic and inelastic components. At this time, we consider only the elastic contribution to this process. We have studied the elastic closure of voids along a fault under normal load using a numerical method. We summarize the basic results of these simulations below.

*Numerical method.* Calculating aperture and normal stress as a function of position on the rough surfaces of

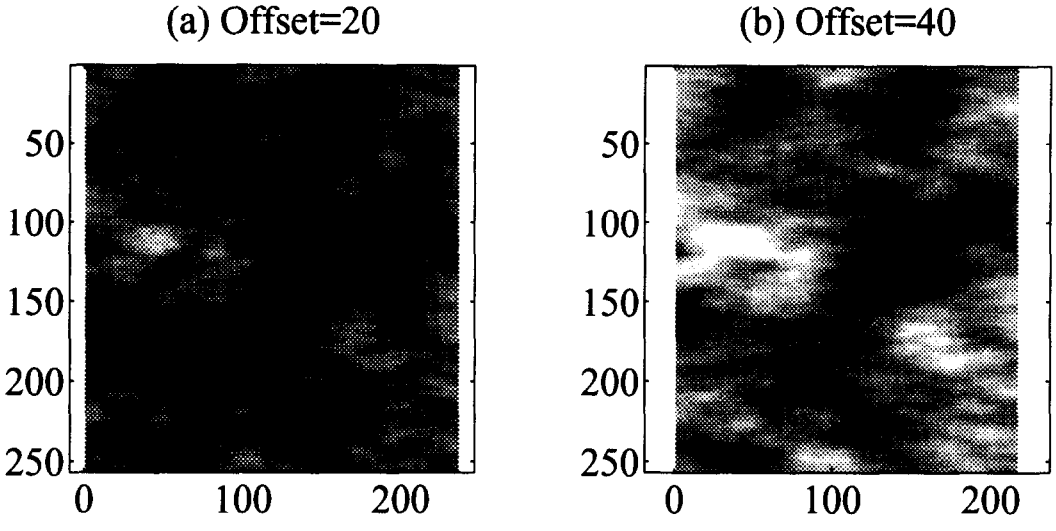


Fig. 5. Examples of aperture or void space created by shear offset of two fractal surfaces ($D = 2.2$) with anisotropy of 3:1. Offset is parallel to the greatest principal axis of anisotropy (horizontal axis on the figures). The scales on the axes are in grid units corresponding to distance (units of length) in the fault plane. (a) Image of aperture distribution for offset of 20 units in a $256 \times 256$ fault. (b) Image of aperture distribution for offset of 40 units. Low to high apertures range from black to white.

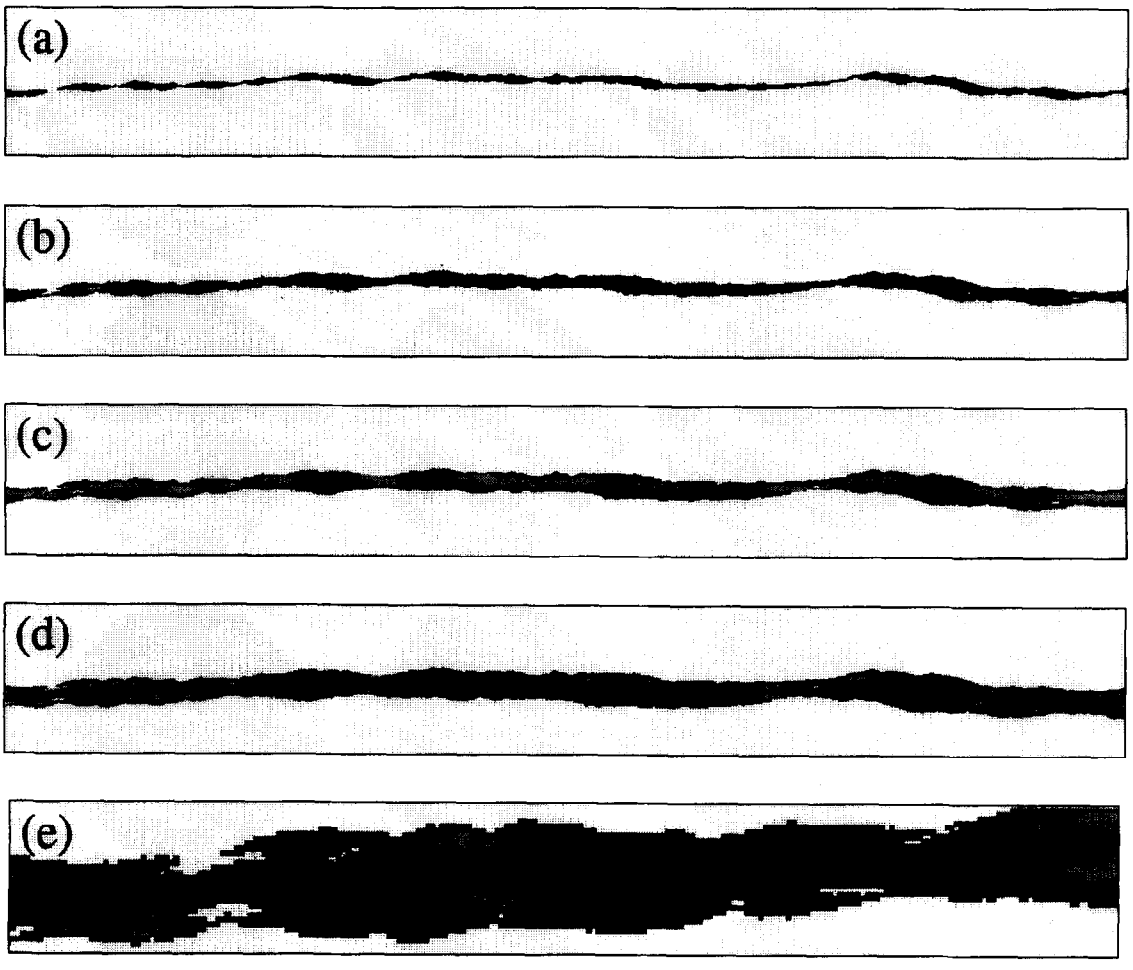


Fig. 10. Cross-section of a vein system. (a–d) Evolution of a composite vein formed by four discrete slip episodes. At each step (a–d) the vein is fractured, the surfaces are slid past one another while the fault dilates, and the resulting open space is filled with vein material. Each sub-vein is assigned a different gray level in the image. (e) Close-up view of the final step (d) showing the complex cross-cutting relationships among the separate vein elements and the entrainment of wall rock.

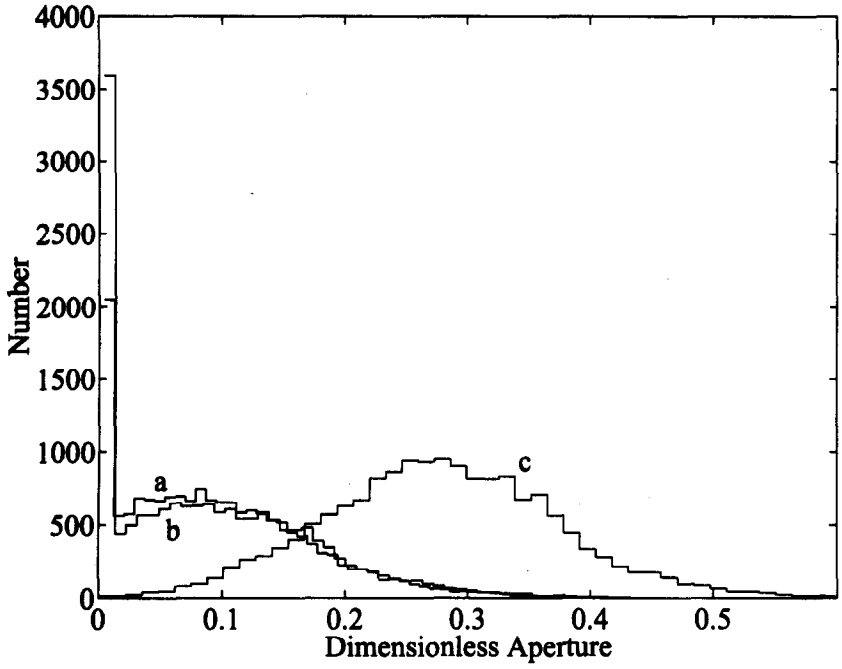


Fig. 8. Example probability density functions of an aperture distribution. Two surfaces with fractal dimension $D = 2.2$ and anisotropy 3:1 were offset by eight grid units and placed in contact. (a) The aperture distribution deformed under normal stress. The aperture was closed by 2 standard deviations from the initial contact. The resulting mean aperture divided by the standard deviation of the original surfaces at length 256 grid units is 0.0951. (b) The aperture distribution formed by simple overlap of the same surfaces without elastic deformation. The surfaces were overlapped to be equivalent to a closure of 2 standard deviations from the initial contact. Negative apertures (overlap) have been truncated to zero. The resulting normalized mean aperture is 0.0918. (c) Original undeformed aperture distribution when the surfaces just contact under zero normal stress.

two contacting elastic solids is a mixed boundary value problem. The problem is non-linear because the regions of different boundary type, open or closed aperture, must be found as part of the solution. This problem can be solved by a numerical relaxation method described first by Andrews (1988) and in greater detail by Brown & Andrews (in preparation).

In the method, two rough surfaces are placed together numerically and regions of overlap are recorded. Since overlap is not physically possible, a stress must be applied at the overlapping regions to bring the surfaces back into contact. Initially the stress at each overlapped point is estimated as being proportional to the amount of overlap. A two-dimensional distribution of contact stresses is thereby determined. A Fourier transform elasticity solution is used to find the actual displacements on a two-dimensional half space due to this stress field. The resulting surface displacements of the half space are subtracted from the topography of the contacting surfaces and a new distribution of overlapping regions is calculated. This procedure is repeated in an iterative fashion until all significant overlaps are removed and further stress change is negligible. The final results of the simulation are the elastically deformed aperture and the spatial contact stress distribution. This numerical method has been compared to the analytic solution of Hertz (Timoshenko & Goodier 1970) for the contact of spherical bodies with excellent results.

*Texture of aperture.* As two surfaces are pressed together under normal stress the aperture distribution closes down and it develops flat regions at the contact areas. These contacts grow in size and the aperture highs between them change shape slightly as the normal stress increases. The deformation can be quantified by looking at the statistics of the aperture as follows.

*Probability density function.* When an aperture distribution is deformed under normal stress the local minima in the aperture become contact points and the surfaces deform locally near these contacts. Before the surfaces touch the aperture distribution is a symmetric 'bell-shaped' curve that closely fits a standard Gaussian curve (Fig. 8c). After contacts form, the distribution becomes truncated at zero aperture and the shape of the curve changes slightly near the contacting end (Fig. 8a). The distortion of the distribution due to fairly significant amounts of contact (in excess of 30% contact area) is minor, with most of the original shape being preserved in the non-contacting areas (compare Figs. 8a and b). Therefore, the distortion of the aperture can be adequately modeled as truncation to zero at the contacting points.

*Normal stress–closure relation.* The elastic model gives a relation between the applied normal stress and the void closure. These results can be expressed in dimensionless form where the normal stress is normalized by the elastic constants and the surface separation is normalized by the standard deviation of the roughness of the original surfaces. Specifically, the dimensionless stress $\bar{S}$ is:

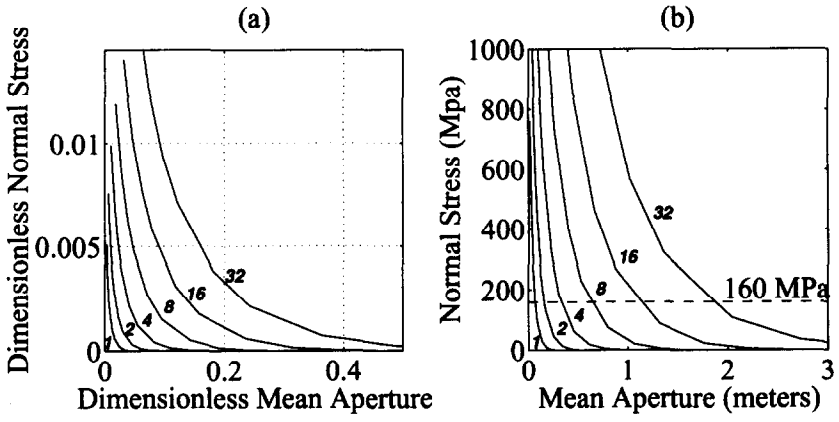


Fig. 9. Normal stress–closure relation for a fault with fractal dimension $D = 2.2$ and 3:1 anisotropy. Labels 1,2,4,8, 16 and 32 represent the amount of shear offset in grid units. (a) Dimensionless plot of normal stress $\bar{S}$ vs aperture $\bar{d}$. See text for definition of these parameters. (b) Curves of (a) scaled to represent a fault in granite with roughness characteristics similar to the Independence Mine Fault: standard deviation of surface over a length scale of 256 m is 5.6 m, shear modulus is $2 \times 10^4$ MPa, and Poisson's ratio is 0.25. The normal stress of 160 MPa (dashed line) would be obtained on a 60° dipping normal fault at approximately 10 km depth. The grid unit and unit of shear offset for (b) is 1 m.

$$\bar{S} = \frac{S_n \cdot \Delta x}{\frac{\mu}{1-v} \cdot \sigma_s^{256}}. \tag{4}$$

The actual normal stress is $S_n$. Length in the fault plane is measured in units of $\Delta x$ and the fault surface is a square of length $256\Delta x$ on a side. The standard deviation of the surface roughness of an individual surface over length $256\Delta x$ is $\sigma_s^{256}$. The shear modulus and Poisson's ratio are $\mu$ and $v$ respectively. The dimensionless mean aperture is:

$$\bar{d} = \langle d \rangle / \sigma_s^{256}, \tag{5}$$

where $\langle d \rangle$ is the mean aperture. Figure 9(a) gives these results in dimensionless form. To rescale these curves to any situation of interest, take the total fault size $L$, compute the standard deviation of the surfaces over this length $\sigma_s^L$, and set $\Delta x = L/256$. Multiply the ordinate by $\sigma_s^L$ and the abscissa by $\mu/(1-v) \cdot \sigma_s^L/\Delta x$. The shear offset on Fig. 9(a) is expressed in integral units of $\Delta x$.

These results show that in general as the surfaces are pressed together the normal stress increases in an exponential manner (Brown & Andrews in preparation). The first item of note is that the fractal dimension has little effect on the normal stress–closure relation. Faults with high fractal dimension are only slightly stiffer than those with low dimension (Brown & Andrews in preparation). Figure 9 shows a series of curves each corresponding to a different shear offset along the fault. When the surfaces are offset in shear, the fault dilates as long wavelength bumps ride over one another. As this dilation occurs, both the amplitude and the wavelength of the important contacting asperities increases, requiring higher normal stress just to maintain a given mean aperture. The point at which the surfaces are touching is indicated where the right-hand edge of each curve reaches the zero stress level. Since the aperture distribution is Gaussian, then the median and the mean are equal and the total range of apertures is about $\pm 3\sigma_a$ from this mean, where $\sigma_a$ is the standard deviation of the aperture. When the surfaces just touch the mean aperture is about $3\sigma_a$ and the maximum aperture is about $6\sigma_a$. For example, on the curve labeled '8' on Fig. 9(a), the mean aperture is about 0.3 when the surfaces just touch, but apertures range from 0 to 0.6 (0.1 is therefore the standard deviation of the undeformed aperture). As the void space is closed under normal stress, then the aperture distribution is truncated to zero and the peak in the bell curve occurs at the smaller aperture value of approximately $3\sigma_a - \delta$, where $\delta$ is the closure.

The results of Fig. 9(a) can be used to determine how much void closure can be expected at a given normal stress for a typical fault. As a fault slips new voids are opened along the fault plane due to the overriding of surface roughness. Scholz (1988) used an approximate (order of magnitude) elastic crack solution to infer that all voids with lengths in the fault plane greater than about 1 cm will be closed by elastic deformation at depths greater than 10 km. Is this possible? Figure 9(b) shows the stress–closure curves rescaled for a fault similar to that associated with the Independence Mine, Alaska. A depth of 10 km is assumed to provide about 160 MPa of normal stress on a normal fault with 60° dip. If we focus on the 8 m shear offset curve, the undeformed mean aperture is about 1.5 m and the total aperture range is 0–3 m (remembering that the undeformed mean aperture is half of the total range). We can see that when this normal load is applied, then the mean aperture decreases to about 0.75 m which means that about 25% of the original total aperture is lost due to elastic deformation. At this point there is still 75% of the original aperture remaining leaving ample pathways for fluid flow. Details of fluid transport properties of void distributions of this type can be calculated using methods discussed by Thompson & Brown (1991) for example.

### *Limits of applicability*

Although the fractal fault model is versatile, there are limits to its general applicability. Obvious shortcomings

are that we have not explicitly incorporated brecciation and gouge formation. Failure of asperities by secondary fracturing at loads above the elastic limit, and the generation of gouge and breccia by wear presumably act to reduce the aperture from that computed in our fault model. These processes are indeed important in natural fault zones (Newhouse 1940, Power *et al.* 1988). For example, Power *et al.* (1988) develop a fractal fault model for gouge and breccia generation that is similar to ours, but focuses on the opposite effect. That is, our model focuses on void space created by 'riding-up' of rough surfaces during shearing, but Power *et al.* (1988) focus on the generation of gouge and breccia layers generated during sliding of fractal fault surfaces in order to model the approximately linear relationship between fault slip and gouge thickness observed in some natural fault zones. Generation of gouge and breccia by wear may significantly reduce the aperture volume from that predicted by our model, but the exact influence of gouge and breccia formation is difficult to predict in detail. Extremely fine-grained gouge packed into void space will almost certainly decrease permeability along the fault, but on the other hand, coarser-grained breccia may act as a proppant, locally holding fault walls apart. Overall, our model will likely give an upper bound to the volume available for both mineral filling and fluid transport. When applying this model to field data it will be important to keep these limitations in mind.

## DISCUSSION

### *Relation of void volume to vein geometry and fluid storage*

Limitations aside, the ability to calculate aperture between fault surfaces as a function of effective normal stress is an important aspect of the fractal fault model with significant implications for predicting vein formation and fault mechanics. Void volume is the product of mean aperture and fault surface area. For a given roughness, amount of slip and applied normal stress, void volume is a sensitive non-linear function of fluid pressure. This arises from the effective stress law ($S_n = S_a - P_f$), where $S_a$ is the applied normal stress due to tectonic and overburden loads and $P_f$ is the fluid pressure. High fluid pressure corresponds to low $S_n$, thicker single-event veins, and presumably veins with greater lateral continuity because of the smaller contact area between fault walls. Thin, discontinuous veins are more likely in low fluid pressure environments. Economic geologists have attempted to correlate vein thickness with ore grade, often with mixed results (e.g. Newhouse 1940, Stoll 1940, Ray 1954, Roscoe 1951, Sanderson *et al.* 1994). Notably, ore deposition from most natural fluids is enhanced by a drop in fluid pressure, particularly if chemical oversaturation is induced by boiling (Guilbert & Park 1985). In the fractal fault model, once steady-state fluid flow was developed, local variations in aperture thickness would give rise to local fluid pressure variations. Along the flow direction as an abrupt opening in void space is encountered, the pressure would drop severely—potentially leading to boiling and/or precipitation of vein filling materials. This might give a positive correlation between vein thickness and ore grade at the length scale of the slip increment.

The spatial distribution, volume, and pressure of fluid stored between fault walls is also important in several models of earthquake mechanics (Sibson 1989, Rice 1992, Byerlee 1993). The fractal fault model allows us to compute directly the volume of fluid stored in void space between rough fault surfaces using the results shown in Fig. 9. Consider a fault with roughness similar to that found in the Independence Mine, Alaska, where the standard deviation of surface topography is 5.6 m over a fault surface with linear dimension of 256 m (Table 1, Fig. 9b). Assume a large earthquake (**M** = 7+) with approximately 4 m of slip at a depth of 10 km. The mean aperture at 160 MPa effective stress (equivalent to hydrostatic fluid pressure at approximately 10 km depth) is about 0.33 m, corresponding to 330 l of fluid per $m^2$ of fault surface, on average. (Note: a 1 mm thick layer of fluid spread over 1 $m^2$ area has a volume of 1 l). If fluid pressure is increased to 0.8 lithostatic (216 MPa), the effective normal stress is approximately 54 MPa and the mean aperture increases to approximately 0.47 m and the fluid volume is increased by a factor of 1.4 to 470 l $m^{-2}$. These types of calculations may be used to constrain a number of different earthquake mechanics model parameters, including estimates of the volume of heterogeneously pressurized fluid trapped in sealed compartments within a fault zone, and the amount of trapped fluid that should be expelled from or drawn into the fault zone following a large earthquake. Such modeling is beyond the scope of this paper, however.

### *Multiple slip model of vein development*

Once the two surfaces have been offset in shear during a slip increment the void space is filled with vein material. The new vein formed will have exactly the same geometry and statistical properties as the aperture. During subsequent slip events the process is the same, with the complications that the fault may not break exactly along the same surfaces as before. Since the surfaces are fractal they have the property that the longest wavelength roughness features also have the highest amplitude. The long-wavelength components of the fault roughness will tend to be more resistant to breakage during slip than the smaller features. Therefore, it is likely that the fault will follow the long-wavelength trends, but may create a new slip surface at finer length scales. To mimic this process, we use a 'phase scrambling' technique alluded to in a previous section in the context of mismatch of rock joint surfaces. At the beginning of each slip event, a new fault surface is generated, which has identical long-wavelength character to the previous slip surface but is different at small wavelengths. To generate this new surface the same random number seed is used for the phase spectrum at

long wavelengths and the same anisotropy factor is used, but the phase spectrum is re-randomized (scrambled) at small wavelengths. The cumulative effect of repeated episodes of slip, filling with vein material and redefinition of the slip surface produces complex vein structures with 'pinch and swell' character and entrained wall rock (Fig. 10). After fault slip accumulates and several new veins are added there is a tendency for the composite vein network (as defined by the outer bounds of vein material) to evolve quickly from a highly sinuous and variable width body to a more tabular geometry (Fig. 10).

*Applications to economic geology*

The fractal fault model produces a three-dimensional vein system that is qualitatively similar to many fault controlled mineral deposits. Features of particular significance include the 'pinch and swell' geometry which is elongated parallel to slip direction, the complex intertwining of veins formed during episodic slip, and incorporation of slices of wall rock (Fig. 10). Success in replicating these key features opens several potential avenues for future research with application to exploration and development of fault-controlled ore deposits.

Fault-controlled ore deposits are marked by a temporal sequence of mineralizing events, which reflect complex variations in fluid temperature, pressure and chemical constituents over time (Guilbert & Park 1985). Ore minerals commonly form during a limited time interval in the total history of faulting and fluid influx. Unraveling the sequential history of mineralization, or mineral paragenesis, provides insight into the timing of mineralization, the relative proportion of vein material which contains ore, and also provides information that is used to guide further exploration within a district. The fractal fault model is conceptually useful in these endeavors.

The tendency for the composite vein network to evolve quickly from a highly sinuous and variable width body to a more tabular geometry as fault slip accumulates and new veins are added to the system has important implications for understanding the distribution of ore based on mapping and sampling by drilling (Fig. 10). Spatial changes in the thickness of the composite vein may greatly underestimate the structural complexity and variability in thickness of individual ore-bearing veins generated during only a small number of slip events. Contradictory evidence for mineral paragenesis based on cross-cutting relationships is a common problem. This type of contradiction is predicted by the fractal fault model. Inspection of the cross-sections in Fig. 10 reveals that although younger veins consistently cross-cut older ones, there is no specific sequence for juxtaposition between veins of different age. At one locale, a vein of intermediate age may separate a younger vein from an older one, but in adjacent regions the sequence of vein juxtaposition may be partially or totally different, and one or more veins may not be present at all. Careful analysis of model cross-sections like those in Fig. 10 is at least conceptually useful, and a thorough statistical analysis of the structural relationships between simulated veins may ultimately provide a quantitative technique for interpreting structural data and estimating paragenesis. Once a mineral paragenesis is established, the fractal fault model may be used to predict the volumetric proportion of ore grade veins, and the amount of gangue vein and wall rock that must be removed during mining. Such data may strongly affect the economic valuation of the deposit. Variations in vein thickness and ore grade encountered in drill holes can also be simulated, and may lead to new strategies for drilling and estimating ore reserves during exploration and mining.

Although the fractal fault model is versatile, we have not explicitly incorporated brecciation and gouge formation. These processes will restrict fluid flow and total fluid volume, yet increase rock–fluid contact area—all of which will affect ore deposition in some way. Additionally, we note that fault intersections are important conduits for fluid flow and mineralization in fault-controlled ore deposits (Knopf 1929, Guilbert & Park 1985). The reader should keep these limitations of the model in mind when evaluating an actual deposit in the field.

*Geostatistics and sampling strategy*

Predicting the structural trends, continuity and thickness of veins in the subsurface remains a fundamental problem for exploration and development of fault-controlled ore deposits. Geologists must rely on geostatistical models of the deposit, which commonly depend upon sampling by drilling. A sampling interval that is too large (beyond the sill in the variogram) results in poor predictions of deposit geometry and grade. Sampling at close intervals increases the ability to predict values between samples, but may severely limit the area of the deposit that can be explored because of drilling costs. Drilling strategy should take the expected properties of the semi-variogram into account. Variograms of fault-controlled vein geometry are anisotropic, with directional variation in the correlation distance mimicing the structural anisotropy of both the veins and fault surfaces (Fig. 7). Our preliminary modeling, which is based on the fault data listed in Table 1, indicates that the drilling pattern should be designed to penetrate the vein in an elongated pattern, with approximately a 2.5:1 ratio in hole spacing between the slip parallel and slip perpendicular directions. The preferred distance between points of penetration is a function of the total amount of fault slip, and should lie within the expected range of the variogram sill (Fig. 7). The geometry of composite vein systems becomes more tabular as slip accumulates than the individual veins generated during a single slip episode (Fig. 10). This means that the variogram for composite vein thickness will be different from that for individual veins, which have a shorter correlation length because of greater geometrical variability (Fig. 7). The variogram for spatial distribution of

ore grade is therefore expected to lie between the variograms of composite and individual vein thickness variability, given the common geological observation that ore deposition usually occurs only during part of the veining history. This qualitative result may prove useful when attempting to constrain predictions of ore grade using a combination of assay and structural data.

Further new work on vein systems is needed to test and refine the fractal fault model. Specific measurements include detailed surveys of vein walls over the spatial range of cm to kms, measurements of the aspect or 'width to length' ratio of both individual and composite veins, and estimates of the void spaced filled by new vein material relative to wall rock and existing vein material that is incorporated by attrition and implosion brecciation and secondary faulting. (e.g. Peters 1993). Scaling between fault displacement and composite vein width is also a crucial parameter, that requires further study in order to calibrate the fractal fault model.

*Acknowledgements*—Portions of this work were performed at Sandia National Laboratories supported by the U.S. Dept of Energy, Office of Basic Energy Sciences, Geosciences Research Program under contract No. DE-AC04-94AL85000. R.L. Bruhn was partly supported by NSF grants EAR-9104677 and EAR-9204835 and U.S. Geological Survey Earthquake Hazards Reduction Program Grant 14-08-0001-G1714. We would like to thank G. Ballantyne, D. Borns, R. Knipe and D. Sanderson for their thoughtful reviews of the manuscript.

## REFERENCES

Andrews, D. J. 1988. On modeling closure of rough surfaces in contact. *Eos, Trans. Am. Geophys. Un.* **69**, 1426.

Båth, M. 1974. *Spectral Analysis in Geophysics*. Elsevier, New York.

Bendat, J. S. & Piersol, A. G. 1971. *Random Data, Analysis and Measurement Procedures*. John Wiley & Sons, New York.

Boullier, A.-M. & Robert, F. 1992. Paleoseismic events recorded in Archean gold-quartz vein networks, Val d'Or, Abitibi, Quebec, Canada. *J. Struct. Geol.* **14**, 161–179.

Brown, S. R. 1995. Simple mathematical model of a rough fracture. *J. geophys. Res.* **100**, 5941–5952.

Brown, S. R. & Scholz, C. H. 1985. Broad bandwidth study of the topography of natural rock surfaces. *J. geophys. Res.* **90**, 12,575–12,582.

Brown, S. R. & Scholz, C. H. 1986. Closure of rock joints. *J. geophys. Res.* **91**, 4939–4948.

Bruhn, R. L., Yang, Z., Wu, D. & Yonkee, W. A. 1991. Structure of the Warm Spring and northern Thousand Springs fault segments, Lost River fault, Idaho: possible effects on rupturing during the 1983 Borah Peak earthquake. *Tectonophysics* **200**, 33–39.

Byerlee, J. D. 1993. Model for episodic flow of high-pressure $H_2O$ in fault zones before earthquakes. *Geology* **21**, 289–304.

Eckel, E. 1949. Geology and ore deposits of the La Plata District, CO. *Prof. Pap. U.S. geol. Surv.* **219**.

Ferguson, H. G. 1927. Geology and ore deposits of the Mogollon mining district, New Mexico. *Bull. U.S. geol. Surv.* **787**, 76–78.

Gilbert, G. K. 1928. Studies of Basin and Range structure. *Prof. Pap. U.S. geol. Surv.* **153**.

Guilbert, G. K. & Park, J. M. 1985. *The Geology of Ore Deposits*. W. H. Freeman, New York.

Knipe, R. J. 1993. The influence of fault zone processes and fault zone diagenesis on fluid flow. In *Diagenesis and Basin Development* (edited by Horbury, A. D. & Robinson, A. G.). *Am. Ass. Petrol. Geol. Stud. Geol.* **36**, 135–154.

Knopf. A. 1929. The Mother Lode system of California. *Prof. Pap. U.S. geol. Surv.* **157**.

Lee, J.-J. & Bruhn, R. L. 1992. Structural anisotropy of normal fault surfaces. *Geol. Soc. Am. Abs. w. Prog.* Rocky Mountain Section Meeting, Odgen, Utah.

Mandelbrot, B. B. 1983. *The Fractal Geometry of Nature*. W. H. Freeman, New York.

Newhouse, W. H. 1940. Openings due to movement along a curved or irregular fault plane. *Econ. Geol.* **35**, 445–464.

Peters, S. G. 1993. Formation of oreshoots in mesothermal gold–quartz vein deposits: examples from Queensland, Australia. *Ore Geol. Rev.* **8**, 277–301.

Power, W. L. & Tullis, T. E. 1991. Euclidean and fractal models for the description of rock surface roughness. *J. geophys. Res.* **96**, 415–424.

Power, W. L. & Tullis, T. E. 1992. The contact between opposing fault surfaces at Dixie Valley, Nevada, and implications for fault mechanics. *J. geophys. Res.* **97**, 14,425–15,435.

Power, W. L., Tullis, T. E. Brown, S. R., Boitnott, G. N. & Scholz, C. H. 1987. Roughness of natural fault surfaces. *Geophys. Res. Lett.* **14**, 29–32.

Power, W. L., Tullis, T. E. & Weeks, J. D. 1988. Roughness and wear during brittle faulting. *J. geophys. Res.* **93**, 15,268–15,278.

Ramsay, J. G. & Huber, M. I. 1983. *Techniques of Modern Structural Geology, Volume* 1: *Strain Analysis*. Academic Press, New York.

Ray, R. G. 1954. Geology and ore deposits of the Willow Creek Mining District, Alaska. *Bull. U.S. geol. Surv.* **1004**.

Rice, J. R. 1992. Fault stress states, pore pressure distributions, and the weakness of the San Andreas fault. In: *Fault Mechanics and Transport Properties of Rocks* (edited by Evans, B. & Wong, T.-F.). Academic Press, New York, 475–504.

Robert, F., & Boullier, A.-M. 1993. Mesothermal gold-quartz veins and earthquakes, In: *Extended Abstracts of NEHRP Conference 'The Mechanical Involvement of Fluids in Faulting'*. U.S. Geological Survey.

Roscoe, S. M. 1951. Dilation maps, their application to vein-type ore deposits. Ph.D. thesis, Stanford University, California.

Sanderson, D. J., Roberts, S. & Gumiel, P. 1994. A fractal relationship between vein thickness and gold grade in drill core from La Codosera, Spain. *Econ. Geol.* **89**, 168–173.

Scholz, C. H. 1988. Critical slip distance for seismic faulting. *Nature* **336**, 761–763.

Scholz, C. H. & Aviles, C. A. 1986. The fractal geometry of faults and faulting. In: *Earthquake Source Mechanics* (edited by Das, S., Boatwright, J. & Scholz, C. H.). *Am. Geophys. Un. Geophys. Monogr.* **37**, 147–155.

Scholz, C. H. & Cowie, P. A. 1990. Determination of total strain from faulting using slip measurements. *Nature* **346**, 837–839.

Sibson, R. 1989. Earthquake faulting as a structural process. *J. Struct. Geol.* **11**, 1–14.

Smith, L., Forster, C. B., & Evans, J. P. 1990. Interactions of fault zones, fluid flow and heat transfer on a basin scale. In: *Hydrogeology of Low Permeability Environments* (edited by Newman, S. P. & Neretnieks, I.). *Int. Assoc. Hydrol. Sci., Select. Pap.* **2**, 41–67.

Stoll, W. C. 1940. Relations of structure to deposition at the Independence Mine, Alaska. *Bull. U.S. geol. Surv.* **933-C**, 201–217.

Thompson, M. E. & Brown, S. R. 1991. The effect of anisotropic surface roughness on flow and transport in fractures. *J. geophys. Res.* **96**, 21,923–21,932.

Timoshenko, S. P., & Goodier, J. N. 1970. *Theory of Elasticity*. McGraw-Hill, New York.

Wu, D., & Bruhn, R. L. 1994. Geometry and kinematics of active normal faults, southern Oquirrh Mountains, Utah: Implications for fault growth. *J. Struct. Geol.* **16**, 1060–1075.